Tracking defect type and strain relaxation in patterned Ge/Si(001) islands by x-ray forbidden reflection analysis

M.-I. Richard,[1,2] A. Malachias,[3] J.-L. Rouvière,[4] T.-S. Yoon,[5] E. Holmström,[6] Y.-H. Xie,[7] V. Favre-Nicolin,[4,8] V. Holý,[9] K. Nordlund,[6] G. Renaud,[4] and T.-H. Metzger[1]

[1]*ID01/ESRF, 6 rue Jules Horowitz, BP220, FR-38043 Grenoble Cedex, France*

[2]*Université Aix-Marseille, IM2NP-CNRS, Faculté des Sciences de St Jérôme, FR-13397 Marseille Cedex 20, France*

[3]*Laboratório Nacional de Luz Síncrotron, C.P. 6192, Campinas, S.P., Brazil*

[4]*CEA-UJF, INAC, SP2M, 17 rue des Martyrs, FR-38054 Grenoble Cedex 9, France*

[5]*Department of Nano Science and Engineering, Myongji University, Yongin, Gyeonggi-do 449-728, Korea*

[6]*Helsinki Institute of Physics and Department of Physics, P.O. Box 43, FI-00014 University of Helsinki, Finland*

[7]*Department of Materials Science and Engineering, University of California at Los Angeles, California 90095-1595 Los Angeles, USA*

[8]*Université Joseph Fourier, Grenoble, France*

[9]*Faculty of Mathematics and Physics, Charles University Prague, Czech Republic*

(Received 14 January 2011; revised manuscript received 24 May 2011; published 9 August 2011)

Plastic relaxation and formation of defects are crucial issues in the epitaxial growth of nanoparticles and thin films. Indeed, defects generate local stress in the crystalline lattice, which affects their surroundings and may lead to undesired effects such as reduced charge-carrier lifetime or nonradiative recombinations. Here, we use a nondestructive method based on x-ray diffuse scattering close to forbidden reflections to identify the defect types with a high sensitivity and quantify their average size and strain field. Combined with transmission electron microscopy, it offers opportunities to track both ensemble average and single defects inside three-dimensional structures. These techniques have been applied to partially embedded and high-Ge-content ($x_{Ge} = 0.87 \pm 0.06$) dots selectively grown in 20-nm-sized pits on Si(001) surfaces through openings in a SiO_2 template. The stress in the 20-nm-wide Ge islands is relaxed not only by interfacial dislocations but also by microtwins and/or stacking faults located at the interface, proving the importance of $\{111\}$ planes and twinning in the relaxation process of nanometer-size Ge dots.

DOI: 10.1103/PhysRevB.84.075314 PACS number(s): 61.72.Nn, 61.72.Dd, 81.07.Ta, 61.72.uf

I. INTRODUCTION

The mechanism of the island formation of Ge on Si(001) via the Stranski-Krastanow growth mode has been extensively investigated by x-ray techniques (see, e.g., Stangl *et al.*[1] for a review). Above a given critical thickness, the misfit strain can no longer be accommodated coherently, and larger islands with interfacial misfit dislocations may appear. Different kinds of defects can be present in Ge islands: screw dislocations, 90° or 60° misfit dislocations, or stacking-faults. Such defects have been extensively studied theoretically[2,3] and experimentally by transmission electron microscopy (TEM)[4,5] to determine their structure, size, and location. Recently, another technique combining the use of chemical etching and atomic force microscopy (AFM) has been exploited[6] to reveal the presence of dislocations inside SiGe islands. However, both methods employ destructive analysis tools. It is, therefore, crucial to realize complementary, nondestructive measurements to study defects inside nanostructures. Additionally, the etching technique[6,7] is material dependent and therefore restricted in its use to Ge islands.

Diffuse x-ray scattering is a well-established method for the investigation of defects in two-dimensional (2D) layers or crystals.[8,9] Although grazing-incidence x-ray in fundamental reflections has been used to infer the presence of defects in Stranski-Krastanow relaxed islands,[10] it could not be used to determine defect types. Recently, a new x-ray method using forbidden reflections made possible the detection of the type of defects, their average size, and strain field inside Si crystals.[11] The diffuse scattering from long-range distortions of the defects is strongly decreased in this case, allowing the direct study of the atomic structure of the defect cores, accessing their crystalline distortion and size. In this paper, we demonstrate that this technique can be employed for the detection of defects inside three-dimensional (3D) nanotructures, for example, Ge quantum dots (QDs) in this work, determining the defect types with high sensitivity and bringing additional information with respect to TEM results.

II. EXPERIMENT

Figure 1 shows the sample preparation process. The investigated sample consists of a Si(001) substrate having hexagonally ordered hole patterns on the surface produced using PS-PMMA (Polystyrene-b-poly-methylmethacrylate) diblock copolymers as illustrated in Figs. 1(a) and 1(b). Such a nanopatterning process can be outlined as follows. Initially, the diblock copolymers form self-assembled hexagonally organized cylindrical patterns.[12] These patterns are transferred to the SiO_2 mask layer through reactive ion etching (RIE) [see Fig. 1(c)], creating 25-nm-wide hexagonally ordered holes separated by ∼45 nm in the oxide layer. Finally, Ge quantum dots are selectively grown at 650 °C in the Si openings by molecular beam epitaxy [see Fig. 1(d)]. The total deposited Ge was equivalent to 4-nm-thick Ge on a bare Si substrate. Selective growth is made possible by Ge adatoms desorbing from the SiO_2 surface with a fraction of them diffusing into the exposed Si areas. After the Ge growth, the SiO_2 layer is selectively etched away by immersion into hydrofluoric acid (HF) solution.[12]

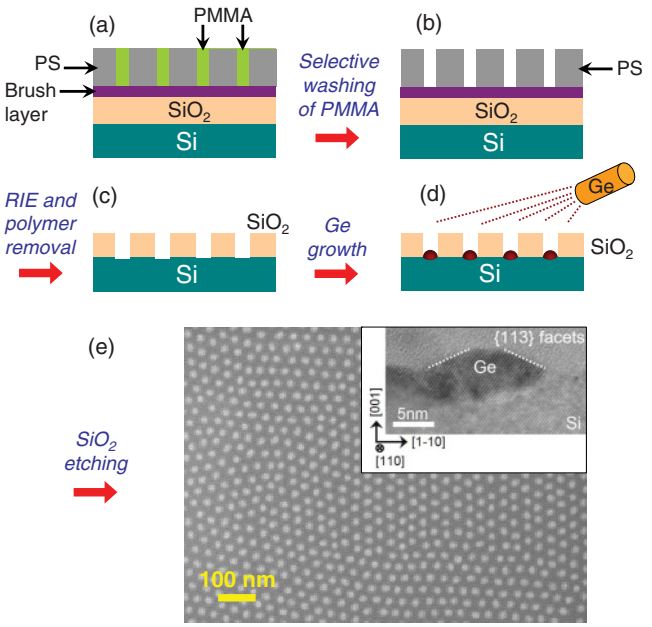

FIG. 1. (Color online) Schematic illustration of the nanopatterning process for forming the self-assembled hexagonal cylindrical patterns of exposed Si areas (holes) in the SiO_2 mask layer using self-assembled diblock copolymer of PS-*b*-MMA as template. (a) Si(001) substrate with diblock copolymers of PS-PMMA, (b) template after selective washing of PMMA, (c) RIE and polymer removal, (d) Ge growth, and (e) scanning electron microscopy image of the grown Ge islands after SiO_2 etching. The inset in (e) shows a HRTEM cross section image in the [110] zone axis of a grown Ge island.

The resulting Ge islands, grown inside overetched ordered patterned Si areas, are long-range hexagonally ordered, inside domains with typical sizes of a few hundred nanometers, as shown in the scanning-electron-microscopy (SEM) image in Fig. 1(e). The inset of Fig. 1(e) displays a high-resolution transmission-electron microscopy (HRTEM) cross-section image in the [110] zone axis of a grown Ge island. HRTEM was conducted using a JEOL 4000 EX field microscope. Sample preparation, including mechanical polishing and ion milling, was needed to reduce locally the sample thickness to about 10 nm. It clearly shows a partly embedded Ge dot. The holes in which the Ge dots have grown have no abrupt vertical edges. The dots are relatively flat with a tendency to show {113} facets and the average QD diameter is about 15–20 nm. The center-to-center distance varies from 34 to 40 nm, leading to a high density of dots of 6.5×10^{10} cm^{-2}, more than one order of magnitude higher than the one observed for Ge nanoislands grown on flat Si(001) substrates.[13] The aspect ratio of individual Ge dots ($\sim$0.33) is comparable to the one of barns and dislocated superdomes and larger than the aspect ratio of coherent pyramids and domes on planar substrates.[14] Such large aspect ratio may be due to the partial embedding of the Ge dots, as revealed by TEM images. This possibly leads to an early onset of dislocations inside these dots of smaller lateral dimensions than dislocated superdomes, making such sample suitable for a structural investigation of defect properties.

Grazing-incidence x-ray diffraction (GIXD) experiments were performed at beamline ID01 (ESRF). A monochromatic

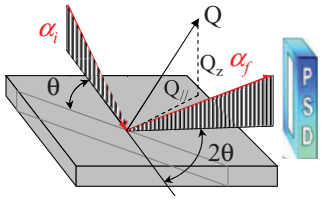

FIG. 2. (Color online) Geometry used to measure the diffuse x-ray scattering at grazing incidence α_i and exit α_f angles with 2θ the diffraction angle. The PSD is used for efficient reciprocal space mapping in the ($Q_{//}$ - Q_z) plane with $Q_{//} = \frac{2\pi}{a_{Si}}\sqrt{h^2+k^2}$ and $Q_z = \frac{2\pi}{a_{Si}}l$.

x-ray beam of 11 keV (wavelength λ of 1.1271 Å) was used. The suppression of the contributions of the higher harmonics of the x-ray beam was achieved by two mirrors. The incident angle was fixed at the critical angle for total external reflection, $\alpha_i = 0.161^\circ$ in order to maximize the diffraction signal from the near-surface region. The exit angle α_f was collected from 0° to 1.5° by a linear position sensitive detector (PSD) perpendicular to the sample surface [see Fig. 2]. All direct or reciprocal space notations refer to the bulk Si unit cell $a_{Si} = b_{Si} = c_{Si} = 5.431$ Å and $\alpha = \beta = \gamma = 90^\circ$. The Miller indexes ($h$, k, and l) are expressed in reciprocal lattice units (r.l.u.) of Si.

III. RESULTS

A. Ordering, composition, and plastic relaxation

Firstly, the strain relaxation, lateral correlation, island size, composition, and mosaic spread of the QDs were investigated by GIXD. Figure 3(a) shows a reciprocal space map around the Si(220) Bragg peak. A broad signal is observed centered around $(h,k) = (1.929, 1.929)$, close to the position of the Ge(220) bulk Bragg peak, expected at $h = k = 1.917$. Regarding to its position and width, the signal is likely to originate from small crystalline structures and is therefore ascribed to the Ge islands. Close to the Si(220) substrate reflection, ordering satellites distributed along noncontinuous correlation rings are observed.

Additionally, linear scans were performed along the angular [1$\bar{1}$0] and the radial [110] directions [see the lines denoted (b) and (c) in Fig. 3(a), respectively]. Angular scans are sensitive to the size and mosaic spread of the islands, which affect the width of the scan profile, whereas radial scans, spanning from Ge to Si reciprocal lattice positions, are sensitive to the strain of the sample.[15] All scans were performed integrating the intensity along the l direction over 1.5° in the exit angle α_f, where $l = a_{Si}/\lambda[\sin(\alpha_i) + \sin(\alpha_f)]$. The angular scan in Fig. 3(b) shows a complex peak structure. The satellites are centered on the Si(220) Bragg peak, demonstrating that correlations arise near the Si substrate/island interface regions. Such an effect is due to the superstructures created by the periodically overetched and strained Si patterns. It contains information about the size and the lateral correlation of the hexagonally ordered and overetched Si hole arrays and thus indirectly about the size and the lateral correlation of the Ge QDs. The observation of up to fourth-order satellites reveals the existence of domains with a long-range ordering of the islands in the sample. From the distance Δh between the (220)Si

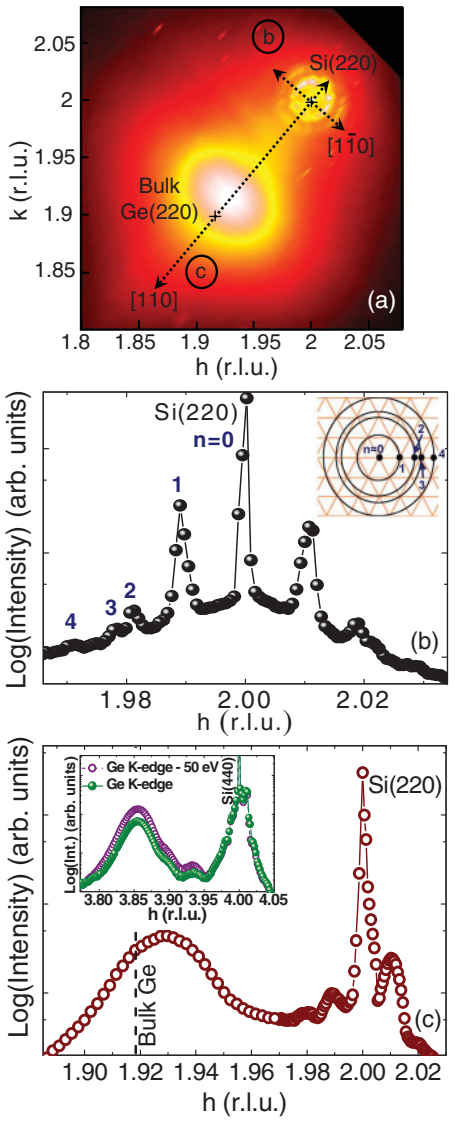

FIG. 3. (Color online) The intensity in the three figures is presented on a logarithmic scale. (a) (220) reciprocal space map of the Ge islands grown on the Si substrate template. The dashed lines labeled (b) and (c) denote the trajectory, along which the line scans in Figs. 2(b) and 2(c) were performed, respectively. The minimum and maximum intensity values are in dark and white, respectively. (b) Angular scan at the (220)Si substrate reflection along the correspondent line denoted in Fig. 2(a). The inset shows a drawing of the hexagonal reciprocal lattice of the organized assembly of islands and the theoretical position of the correlation peaks (black circles). (c) Radial scan close to the (220)Si substrate reflection along the correspondent line denoted in Fig. 2(a). The inset displays radial scans around the (440)Si Bragg peak measured below (−50 eV) and at the Ge K edge ($E = 11103$ eV).

Bragg peak ($n = 0$) and the first ordering peak ($n = 1$), the average inter-pit distance of the hexagonally packed islands is $D = a_{\mathrm{Si}}/(\sqrt{2}\Delta h) \sim 38$ nm, which is in a good agreement with the SEM analysis. The distance between the nth ordering peak and the $(n-1)$th ordering peak corresponds to a hexagonal ordering averaged in rotation [see the inset in Fig. 3(b)]. Nevertheless, the presence of discrete peaks in Fig. 3(a) reveals some preferential ordering directions within the sample area probed by x rays. This hexagonal lateral ordering is composed of domains with size inversely proportional to the full width at half maximum (FWHM) of the correlation peaks. This leads to ordered domains of ∼190 nm lateral size, which is in a good agreement with the SEM image shown in Fig. 1(e). On the radial scan along the [110] direction and close to the Si(220) substrate reflection [see Fig. 3(c)], correlation peaks are also well-observed around the Si Bragg peak. Such peak structure has an intensity profile that is asymmetric with respect to the sharp (220) substrate peak: the center of mass of the correlation rings is slightly displaced toward the high-h side of the Si Bragg peak. This is consistent with the fact that islands are surrounded by Si atoms under compressive strain since higher values in a reciprocal space imply smaller lattice parameters, i.e., compression.

Despite the deposition of nominally pure Ge, alloying with Si atoms from the substrate is known to take place during growth at 650 °C.[16] Quantifying the average Ge composition x of the dots is therefore mandatory to correctly evaluate their strain with respect to a fully relaxed bulk $\mathrm{Ge}_x\mathrm{Si}_{1-x}$ alloy. To determine the average composition of the Ge dots, anomalous grazing incidence diffraction using multiwavelength anomalous diffraction (MAD)[17,18] was performed. The inset of Fig. 3(c) shows radial scans measured for selected energies near the Ge K edge around the Si(440) reflection. Taking advantage of the Ge anomalous effect, the Ge composition inside the nanostructures[19] can be determined without any model assumption. MAD measurements near the Ge K-absorption edge lead to an average Ge composition of (0.87 ± 0.06) in the islands. Compared to domes grown on flat Si(001) substrates, which have an average Ge content of ∼60–70% at 650 °C,[16] the high Ge content can be here ascribed to the reduced Si surface diffusion due to the presence of a large fraction of oxide-covered areas in the patterned sample during the Ge growth. The average lattice parameter of the dots is calculated from the h position of the SiGe scattering determined by GIXD: $a_{\mathrm{dot}} = 5.628$ Å (using $h_{\mathrm{dot},440} \sim 3.855$). The lattice parameter of a relaxed (zero-stress) $\mathrm{Si}_{1-x}\mathrm{Ge}_x$ alloy of composition x (∼0.87) is ∼5.625 Å, taking into account the deviation of the SiGe alloy lattice constant from the Vegard's law. To determine how much the unit cell is stressed in comparison with the relaxed one, the in-plane dot strain can be calculated with respect to a fully relaxed bulk $\mathrm{Si}_{1-x}\mathrm{Ge}_x$ alloy as $\epsilon_{//} = \frac{a_{\mathrm{dot}} - a_{\mathrm{Si}_{1-x}\mathrm{Ge}_x}}{a_{\mathrm{Si}_{1-x}\mathrm{Ge}_x}} \sim (0 \pm 0.2)\%$, leading to a degree of relaxation $R = (a_{\mathrm{dot}} - a_{\mathrm{Si}})/(a_{\mathrm{Si}_{1-x}\mathrm{Ge}_x} - a_{\mathrm{Si}}) \sim 1$. This demonstrates that the material inside islands can be considered as a relaxed (zero-stress) alloy within the precision of our measurements.

In Fig. 3(c), the broadening of the diffuse scattering from the Ge islands is related to the small island size and to a nonconstant strain field in the Ge dots. The observed full relaxation of these $\mathrm{Ge}_x\mathrm{Si}_{1-x}$ islands can only be explained by plastic relaxation. To demonstrate this, we performed finite-difference method (FDM) simulations; assuming a coherent, i.e., pseudomorphically strained, island of even pure Ge and of 20 nm width, the in-plane strain was calculated and the scattered intensity was simulated. It was found to peak at 1.96, much closer to the Si peak than actually was found ($h = 1.929$) [see Fig. 3(c)]. A similar drift of the island peak was observed

in incoherent InAs/GaAs islands.[10] This demonstrates that the experimentally observed relaxation cannot be achieved by coherent elastic relaxation and that these islands can be identified as plastically relaxed dots. In the inset of Fig. 3(c), intermediate peaks in-between the Ge and Si Bragg peaks are observed. These satellites may arise from interfacial dislocations[20–22] that are out of the scope of this manuscript and may be further explored in a future work.

The widths of the Ge peaks δq_r measured in radial scans for several orders allow estimating the distribution of interplanar distances δd_{hkl} inside the islands and the average island size L according to $\delta q_r^2 = (\frac{\delta d_{hkl}}{d_{hkl}})^2 q_r^2 + (\frac{2\pi}{L})^2$,[23] where $q_r = \frac{2\pi}{a_{\mathrm{Si}}}\sqrt{h^2+k^2+l^2}$. Knowing L, the in-plane mosaic spread M can be inferred from the width Δh of angular scans according to $(\frac{\Delta h}{h})^2 = M^2 + \frac{1}{2h^2}(\frac{a_{\mathrm{Si}}}{L})^2$. This yields $M = 0.8°$, $L \sim 17$ nm and $\frac{\delta d_{hkl}}{d_{hkl}} \sim 0.014$.

B. Investigation of defects by HRTEM

Further complementary analysis of island relaxation was made possible by performing HRTEM, which gave hints on the defect location in different dots. An HRTEM image of a Ge island taken along the [110] zone axis is shown in Fig. 4. The island was analyzed by the geometrical-phase-analysis (GPA) method.[24] Figure 5 illustrates the phase suppression outside the sample using the GPA method. The method allows to have more direct and quantitative results. For instance, by directly giving lattice-parameter maps [see Figs. 4(d) and 4(e)], the shape of the dots can be estimated. It is found that the internal side interfaces of the Ge dots tend to follow {111} planes. Phase maps [see Figs. 4(b) and 4(c)] are also a simple way to detect dislocations with an edge component perpendicular to the direction of observation. Figures 4(b) and 4(c) display two phase maps obtained by selecting two nonparallel reciprocal lattice vectors **g**: $\mathbf{g} = (\bar{1},\bar{1},1)$ and $\mathbf{g} = (1,\bar{1},1)$. When the Burgers vector of a dislocation has a component along the selected **g** vector, the phase map contains a curved segment whose phase shows a jump of 2π. This segment starts at the dislocation core and finishes either at another dislocation core or at the surface of the crystal. By varying the origin of the phase, the orientation of the discontinuity segment varies and rotates around the dislocation core. This means that the ending point of this discontinuity segment in the crystal precisely gives the location of the dislocation core. Once the dislocation cores are located, a Burgers circuit, like in Fig. 4(a), can be drawn to extract the exact projected Burgers vectors. In Fig. 4(a), only one dislocation is clearly observed at the center of the island basis. Its projected Burgers vector is equal to $\frac{1}{2}[\bar{1}10]$. As this type of Burgers vector is quite common in Si, it is supposed to have no out-of-plane component. However, from this image, it is not possible to determine if the observed dislocation is a 60° dislocation with a dislocation line along $[\bar{1}01]$ or a 90° dislocation with a dislocation line along [110]. Most of the time, one dislocation was observed at the center of the dots. But two dislocations (in large dots) or no dislocation (in smaller dots, but this could be due to the fact that the dot has been cut during TEM preparation and that only the part of the dot containing no dislocation is visualized) were observed in a few dots.

It is interesting to evaluate if the lattice parameters calculated in Figs. 4(d) and 4(e) are coherent with the number of dislocations found. For instance, Fig. 4(d) [Figure 4(e)] indicates (111) interplane distances inside the Ge island of $d_{111,i} = 0.329$ nm (0.328 nm) and inside the Si substrate of $d_{111,s} = 0.318$ nm (0.314 nm). In order to accommodate this misfit between {111} planes, a supplementary {111} plane in Si is needed every n {111} planes, where n is given by the equation $d_{111,s} = n \times (d_{111,i} - d_{111,s})$. The distance between two dislocations at the interface should be equal to $\Lambda = n \times d_{111,s}$ or ~7–9 nm. Such value can also be obtained, as an average, from x-ray measurements. Indeed, the in-plane distance Λ is given by the relation $\Lambda = b/f$, where $b = a_{\mathrm{Si}}/\sqrt{2}$ is the norm of the projected $\frac{1}{2}[\bar{1}10]$ Burgers

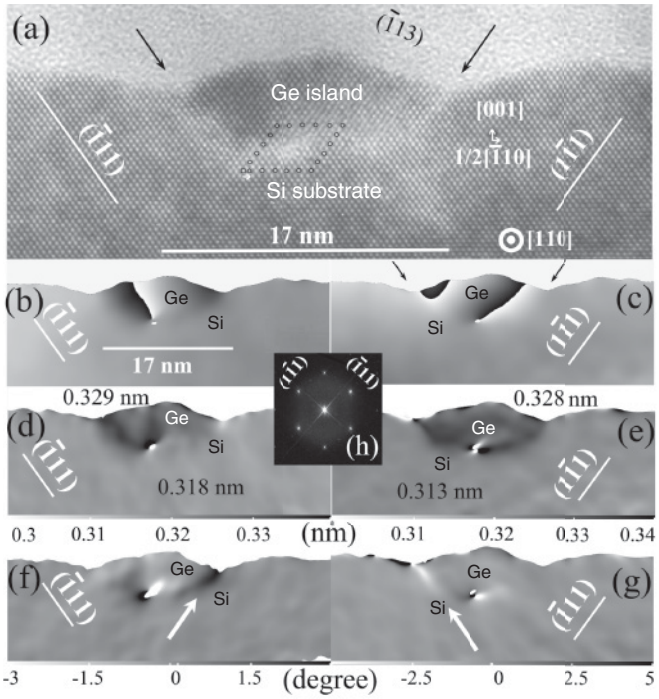

FIG. 4. HRTEM cross-sectional images taken along the [110] zone axis and associated geometrical phase images. (a) Initial HRTEM image. A Burgers circuit has been drawn around the dislocation located at the bottom Ge/Si interface. The Burgers vector of the dislocation is $\frac{1}{2}[\bar{1}10]$. The black arrows point to the {111} Si/Ge interfacial planes. (b) and (c) Geometrical phase images obtained with selected **g** vectors equal to $(\bar{1},1,1)$ and $(1,\bar{1},1)$, respectively. The phase images contain discontinuities that ends either at the surface or at a dislocation core. The phase outside the sample in the glue part (at the top) has been set to zero by using a mask computed from the phase image (see Fig. 5). (d) and (e) {111} lattice parameter maps obtained respectively with the $(\bar{1}11)$ [see Fig. 3(d)] and $(1\bar{1}1)$ [see Fig. 3(e)] **g** vector. The average values of the interatomic distance between (111) planes inside the Si substrate (noise changes the reference value of 0.314 nm for the Si {111} interplane distance) and in the center of the Ge dot are written. (f) and (g) {111} angle maps obtained respectively using the $(-1,1,1)$ [see Fig. 3(f)] and $(1,-1,1)$ [see Fig. 3(g)] **g** vectors. The local angles measure the local rotation of the {111} planes. (h) Numerical power spectrum used in the GPA analysis to select a given **g** diffraction spot with an aperture.

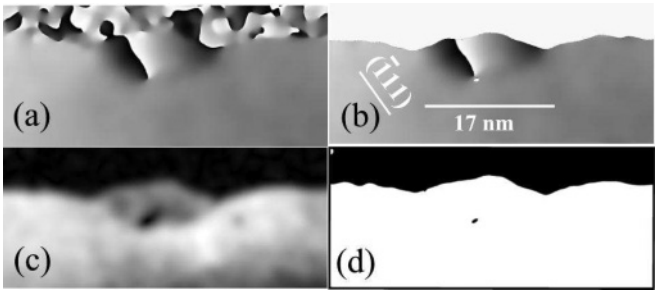

FIG. 5. Illustration of phase suppression outside the sample. (a) Original phase image. The phase in the glue part is just random noise and prevents to see clearly the dot. (b) Phase image after noise suppression. One can notice that the discontinuity at the right side of the dot just falls at the boundary between the glue and the dot. (c) Original amplitude image obtained with GPA. (d) Binary mask (0 and 1) obtained by thresholding the amplitude image.

vector of the interfacial dislocations found by TEM and f is the lattice parameter misfit $f = (a_{\text{dot}} - a_{\text{Si}})/a_{\text{dot}}$, where a_{dot} is the average in-plane lattice parameter of the Ge dots. This leads to $\Lambda \sim 11$ nm. X-ray diffraction and high-resolution transmission electron microscopy give the same order of magnitude. In Fig. 4, the size of the dot is about 17 nm, so there should be 17 nm/Λ or $\sim$2 dislocations at the Si/Ge interface if all the observed misfit was due to misfit dislocations. As indicated in Fig. 4, there is only one dislocation at the bottom part of the dots, we conclude that the strain in these small-size dots is not entirely relaxed by misfit dislocations and additional defects have to be introduced.

If one looks more closely at the phase image in Fig. 4(c), one notices that a small discontinuity appears at the top left part of the Ge dot. This small discontinuity segment starts and ends at the surface and cannot be directly attributed to a dislocation core. The angle maps [see Figs. 4(f) and 4(g)], showing how a given lattice plane **g** is rotated, are ways to image the disturbed parts of the island. It is found that deformed regions are not only situated near the dislocation core but are also located at the top side parts of the dots. These deformed areas tend to follow {111} planes. Some images, like Figs. 6(a) and 6(b), show that these top-side {111} parts contain defects that cannot be clearly identified in these projected images. However, as it will be confirmed by x-rays, one can notice some tendencies to form {111} stacking faults or small twins in these regions.

C. Defects and stress relaxation via x-ray analysis of forbidden reflections.

The x-ray results presented in the previous sections were obtained close to allowed Bragg reflections, around which the investigation of the structure of planar defects inside 3D islands is either difficult or impossible: the scattering contribution of defects inside 3D dots is weak due to the small number of atoms forming the defect and is thus hidden by the broad diffuse scattering from the nanostructures. In this section, we show that grazing incidence diffuse x-ray scattering (GI-DXS) around bulk *forbidden* reflections can be employed to detect defects inside 3D nanotructures, determining the defect types with high sensitivity and bringing additional information with respect to TEM results and standard x-ray scattering

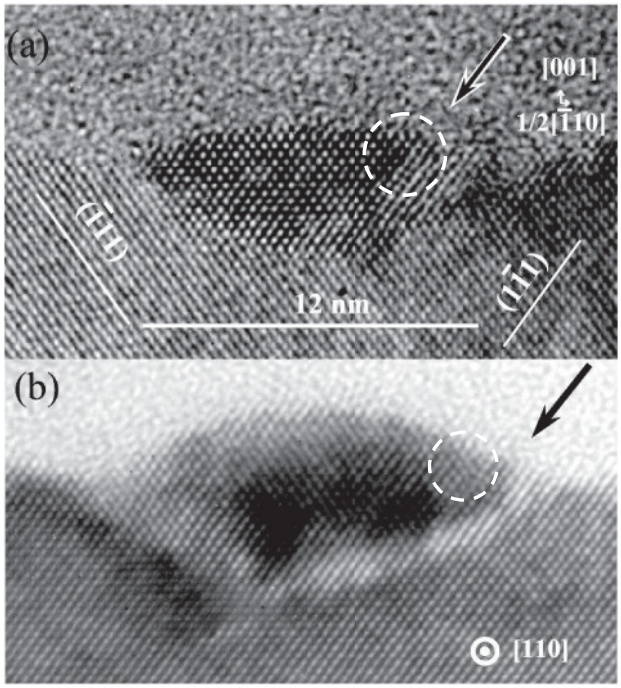

FIG. 6. HRTEM images of two Ge dots that contain defects on one side of their {111} interfaces as indicated by the arrows and the white circles.

measurements. The diffuse scattering from the distorted long-range neighborhood of the defects is strongly reduced in this case, which makes it possible to study the structure of the core of defects. This technique has been recently successfully applied in the case of implanted Si substrates[11] and has allowed to determine the size and the compression at the core of stacking faults.

Figure 7(a) displays a part of the 3D intensity distribution around the (200) reciprocal space position, where the l direction represents the intensity distribution along the linear detector. The scattered intensity is concentrated in streaks along ⟨111⟩ directions. In Fig. 7(b), the intensity was integrated along l, i.e., along the [001] direction. Consequently, the integrated hump-like intensity follows the projected ⟨110⟩ directions in the plane. According to previous studies and theoretical predictions,[25] the intensity concentrated in streaks along ⟨111⟩ is a characteristic footprint of the presence of faulted dislocation loops (FDLs), either composed of stacking faults (SFs) or twin faults. In a diamond structure, the stacking sequence in the ⟨111⟩ direction is generally denoted . . .*AaBbCcAaBbCc*. . ..[26] Stacking- faults result from the incorporation or removal of a double plane in the usual stacking sequence. More precisely, extrinsic SFs consist of two extra {111} planes, bounded by Frank loops with Burgers vectors $\mathbf{b} = a/3\langle 111\rangle$ (see Ref. 26). The size t_0 of the double inserted plane along the ⟨111⟩ direction has the nominal distance $\Delta_0 = a\sqrt{3}/4$. Like stacking faults, twins are caused by destroying the stacking sequence in the ⟨111⟩ direction of the crystal. The stacking sequence . . .*AaBbCcAaBbCc*. . . of {111} planes is changed to . . .*AaBbCc**BbAaCc*. . .. Although stacking faults are planar defects and twins are volume defects, there are close relationships between {111} stacking faults

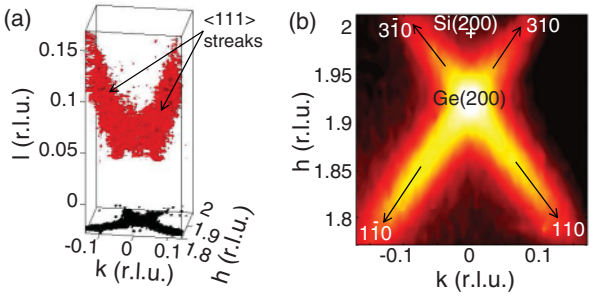

FIG. 7. (Color online) (a) Three-dimensional intensity distribution around $\mathbf{h} = 2$. The scattered intensity, which is represented on a logarithmic scale, is concentrated in streaks along ⟨111⟩ directions, perpendicular to the fault planes. (b) In-plane reciprocal space map of diffuse scattering measured around the Si basis-forbidden reflection (200). The intensity, which is displayed on a logarithmic scale, was measured by a position sensitive detector collecting the diffracted signal between $\alpha_f \sim 0°$ and $\alpha_f \sim 1.5°$. The minimum and maximum values are in dark and white, respectively.

and {111} twins: they often have a common origin, twins are necessarily bounded by SFs and an association of SFs creates a volume defect that can contain microtwins. From symmetry considerations, it follows that the reciprocal space distribution of the intensity scattered by stacking faults or twins, what we call hereafter an association of {111} stacking faults or shortly defects on {111} planes, is concentrated along ⟨111⟩ lines. Thus the streaks along the ⟨111⟩ directions reveal the presence of stacking faults or twins on {111} planes inside the Ge islands. No atomic ordering of Si and Ge atoms, which would also give rise to nonzero intensity near the (200) reflection, is observed in this sample due to the low interdiffusion as indicated by the lack of the double-peak feature observed in Malachias *et al.*[27]

The gaussian fit of the cross section of the measured streak gives the mean thickness $t_0 = (6.5 \pm 0.5)$ nm of the faults. In Fig. 7(a), the four streaks intercept each other at $h_{\mathrm{Ge},200} = 1.925$. At this position, a maximum of intensity is observed. The (400) reflection was measured for comparison with the (200) data. The intersection of the four streaks corresponds to the position of the maximum of relaxation ($h_{\mathrm{Ge},200} = 1.925 \equiv h_{\mathrm{Ge},400}/2$) of the Ge QDs measured at the (400) reflection. This evidences that the intensity observed at $h = 1.925$ arises from a basis-forbidden reflection from material inside the relaxed islands.

Figure 8(a) displays the experimental integrated defect-induced intensity along the ⟨111⟩ rods linking the $(1\bar{1}1)$Ge and (311)Ge Bragg peaks and passing through the (200)Ge reciprocal space position. Additional peaks are observed at noninteger values of h, k, and l: $\frac{1}{3}(5\bar{1}1)$ and $\frac{1}{3}(822)$. The diffraction profile observed for stacking faults [see Fig. 9(b)] does not exhibit the characteristic extended intensity distribution observed here. The appearance of these additional peaks demonstrates that the defects are more complex than single stacking faults and are the consequence of twin faulting on {111} planes.[20]

In order to understand the extended reciprocal space footprint of twins, let us consider a twin fault as sketched in the inset of Fig. 8(b). Crystal 1 is the twin or mirror of

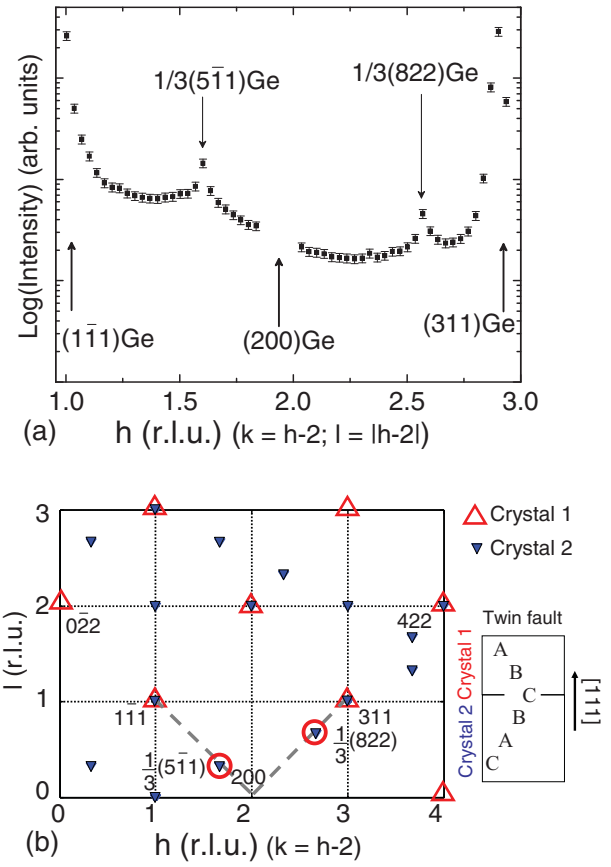

FIG. 8. (Color online) (a) Measured integrated intensity (logarithmic scale) along ⟨111⟩ rods passing through the $(1\bar{1}1)$Ge, (200)Ge, and (311)Ge Bragg peaks. A part of the signal was not collected in the vicinity of the (200)Ge reciprocal space position due to limitations of the used scattering geometry. (b) Reciprocal space map of crystal twinning. The $(1\bar{1}0)$ plane is drawn: all the peaks verify $h - k = 2$. The fourfold symmetry around the [001] direction has been taken into account. The Bragg peaks of the direct and indirect stackings are symbolized by a red Δ and a blue ∇ markers, respectively. The experimentally observed twin Bragg peaks at $\frac{1}{3}(5\bar{1}1)$ and $\frac{1}{3}(822)$ are circled in red.

crystal 2. The corresponding transformation is described by the matrix[28]

$$\mathbf{S} = \begin{pmatrix} -1/3 & 2/3 & 2/3 \\ 2/3 & -1/3 & 2/3 \\ 2/3 & 2/3 & -1/3 \end{pmatrix}.$$

In the reciprocal space related to crystal 1, the Miller indexes (h_1, k_1, l_1) of the Bragg peaks fulfill $h_1 + k_1 + l_1 = 4n$ or h_1, k_1, and l_1 are odd. In the reciprocal space of crystal 2, the Miller indexes (h_2, k_2, l_2) of the Bragg peaks are related to h_1, k_1, and l_1 by the following relations obtained via the matrix:

$$\begin{cases} h_2 = 1/3(-h_1 + 2k_1 + 2l_1), \\ k_2 = 1/3(2h_1 - k_1 + 2l_1), \\ l_2 = 1/3(2h_1 + 2k_1 - l_1). \end{cases}$$

For twinning crystals, the reciprocal space is thus composed of (h_1, k_1, l_1) Bragg peaks from crystal 1 (direct stacking:

AaBbCc) and of (h_2, k_2, l_2) Bragg peaks from crystal 2 (indirect stacking: *CcBbAa*). Figure 8(b) displays the Bragg peaks of the direct stacking symbolized by red Δ labels (crystal 1) and the additional Bragg peaks of the indirect stacking symbolized by blue ∇ labels (crystal 2). The figure takes into account the four types of orientations of the twin faults. Among the additional Bragg peaks, the $\frac{1}{3}(5\bar{1}1)$ and $\frac{1}{3}(822)$ reflections are observed, demonstrating that the additional peaks in Fig. 8(a) result from the presence of twin faults. From the full width at half maximum of the additional peaks along the ⟨111⟩ direction, the average size of the twin faults along the ⟨111⟩ direction can be inferred. The low resolution in the region of the peaks does not allow us to give a value for the average size of the twin faults.

We have compared the intensity distribution along the ⟨111⟩ directions with the result of atomistic simulations. The equilibrium atomic structure of a pure, uncapped Ge island on top of a Si substrate was calculated using the well-tested Stillinger-Weber interatomic potential model.[29] The dimensions of the substrate were $40 \times 40 \times 20\ \text{nm}^3$ and the Ge island was a semi-ellipsoid of 10 and 8 nm for the semimajor and semiminor axes, respectively. Using the positions of atoms following from the atomistic simulations, the x-ray scattering was calculated using the method depicted in Nordlund *et al.*[30] Qualitatively, the simple shape chosen for the simulated island does not influence the obtained results. In Fig. 9(a), we have plotted the distributions of the Si and Ge scattered intensities ($|F_{\text{Si}}|^2$ and $|F_{\text{Ge}}|^2$) calculated along the ⟨111⟩ rods linking the $(1\bar{1}1)$Si and (311)Si Bragg peaks and passing through the

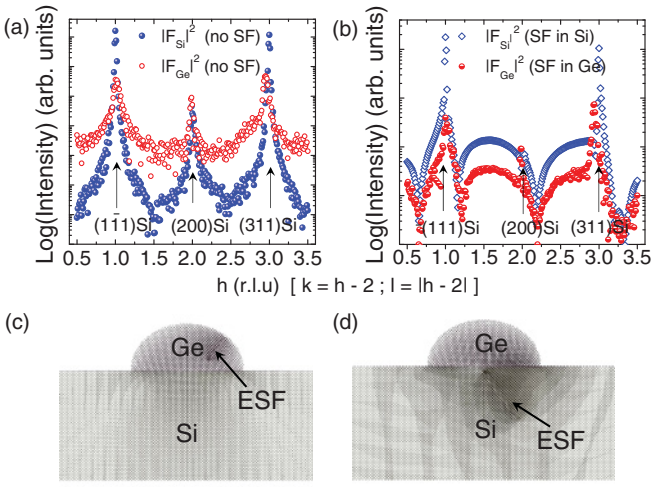

FIG. 9. (Color online) (a) Si and Ge scattered intensities ($|F_{\text{Si}}|^2$ and $|F_{\text{Ge}}|^2$) calculated along the ⟨111⟩ rods linking the $(1\bar{1}1)$Si and (311)Si Bragg peaks and passing through the reciprocal space lattice point $\mathbf{h} = (200)$ for a pure and defect-free Ge dot grown on a Si substrate. (b) Simulated $|F_{\text{Ge}}|^2$ intensity scattered by a Ge dot having a single stacking-fault, with the Si substrate free of defects [see Fig. 9(c)] and the simulated $|F_{\text{Si}}|^2$ intensity scattered by the Si substrate containing one single stacking fault, with a defect-free Ge island [see Fig. 9(d)]. The atomic positions inside the Ge dot and the Si substrate were obtained by atomistic simulations. Qualitatively, the simple shape chosen for the simulated islands does not influence the obtained results.

forbidden reciprocal lattice point $\mathbf{h} = (200)$ for the defect-free Ge dot grown on a Si substrate. Note that intensity at the (200) reflection is due to truncation effects of the simulated scattering objects (substrate, islands). In a small volume, the forbidden diffraction can be strong due to the truncation effects. Figure 9(b) shows the simulated $|F_{\text{Ge}}|^2$ intensity scattered by a Ge dot having a single stacking fault with the Si substrate being free of defects [see Figure 9(c)]. The simulated $|F_{\text{Si}}|^2$ intensity scattered by the Si substrate containing one single stacking fault [Figure 9(d)] with a defect-free Ge island is also shown in Figure 9(b). The single extrinsic stacking fault was created by adding an extra double (111) atomic plane in the center of a large simulation cell. The extra plane had the shape of a regular hexagon bound by a dislocation line segment along ⟨111⟩ crystal directions. From the results of Figs 9(a) and 9(b), it follows that the Si and Ge scattered intensities around the forbidden reciprocal space lattice point $\mathbf{h} = (200)$ can effectively vary depending on the presence of defects, which causes changes in the interplanar distances. Note that significant intensity is observed exactly at the forbidden (200) position even for unfaulted and/or unordered islands, which in this case arises from the truncation of the unit cells at the substrate and island surfaces in our simulation, indicating that measuring intensity at the (200) position does not directly imply ordering or faults and always requires proper analysis. Contrary to a single extrinsic stacking-fault, no pronounced minimum is experimentally observed around $\mathbf{h} = (200)$. Single stacking-faults lead to minima explained by stacking interferences along ⟨111⟩ directions. These interferences are modulated by the width of the stacking faults whereas twins lead to twinning peaks. The fact that no minimum is experimentally observed reveals that the defects in the sample are predominantly twin faults.

IV. DISCUSSION

Diffuse x-ray scattering around forbidden reflections reveals that the sample contains an accumulation of {111} defects, which are composed of microtwins and stacking faults. Here, the formation of dots is completely different from the expected conventional Stranski-Krastanow mode. The deposition of Ge inside the SiO_2 hole, prevents the creation of a wetting layer. Contrary to Ge islands grown on flat Si(001) surfaces, which have been reported to introduce dislocations when the base diameter exceeds about 100 nm[31,32] and to undergo an advanced plastic relaxation compared to the ones grown on pit-patterned Si(001) substrates,[33] these Ge dots already show {111} defects and dislocations in spite of their small size of 15–20 nm. The appearance of dislocations may result from the limited elastic relaxation due to the confined patterned structure. This indicates that the pitted geometry inhibits elastic relaxation of misfit strain resulting in the lowering of the apparent dislocation nucleation barrier. Different mechanisms can be invoked for the creation of the {111} defects. (i) Yoon *et al.*[34] reported that multiple Ge islands can first form inside each single exposed Si area and then coalesce into a single island. Twins or stacking faults can be created at the intersection of the different grains to accomodate the misalignment of two Ge islands during

the coalescence process.[35] The twins nucleate at the Ge-Si interface and propagate to the Ge surface along one of the ⟨111⟩ planes. In the present sample, no grains were observed in the dots by TEM. This indicates that coalescence of neighboring islands is certainly not at the origin of the observed {111} defects in this sample.

(ii) A second mechanism could be the following. As also reported by Yoon *et al.*,[34] the Si holes are overetched by at least 5 nm leading to a Si surface with craters. As shown in Yoon's work (see Fig. 4 in Ref.[34]), the overetched regions contain {111} side facets and {001} bottom facets. During growth, the Ge atoms fill the Si holes: the interfaces between Si and Ge will tend to follow {111} planes on the side of the dots and (001) plane at the bottom. As shown in the TEM images in Fig. 6, {111} defects are localized at the Si/Ge {111} interfaces. There are little chances that {111} stacking faults are the defects that minimize the plastic energy as generally misfit dislocations are preferred. The presence of defects on {111} facets could be due to the incomplete surface cleaning. During the growth process, the exposed Si surfaces are surrounded by oxides and recessed in nanometer-dimension holes. The *in situ* surface-cleaning technique before Ge growth, which consists of heating the sample under a low Si flux, is possibly insufficient for complete removal of SiO or SiC clusters, which are known to lead to stacking faults. These results highlight the important microstructural issues and growth behavior of quantum dots grown on patterned substrates prepared by diblock copolymer nanopatterning.

V. CONCLUSION

In summary, we have demonstrated that diffuse x-ray scattering around a forbidden reciprocal lattice point is well suited for the study of planar faults (stacking faults) and twin faults in nanostructures. The diffuse scattering from the distorted long-range neighborhood of the defects is fairly suppressed in this case, which makes it possible to study the structure of the core of defects. Thanks to the association of this technique with HRTEM, the mechanism of plastic stress relaxation in these dots has been determined. The stress between the Ge dot and the Si matrix is relaxed not only by interfacial dislocations but also by {111} defects located on the lateral Si/Ge interfaces. These {111} defects are composed of an association of stacking faults and twins. Diffuse scattering appears as a fine and destruction-free technique to determine the defect type, strain, and size in nanostructures. This developed x-ray method can also be combined with *in situ* growth to detect, for example, the exact onset of formation of stacking faults inside nanostructures.

ACKNOWLEDGMENTS

All experiments were performed at beamline ID01 at the ESRF, we are very grateful to the ID01 staff and J. Coraux for their help during experiments. M.-I. R. acknowledges Tobias Schülli for fruitful discussions and C. Priester for the development of the FDM program.

[1] J. Stangl, V. Holý, and G. Bauer, Rev. Mod. Phys. **125**, 725 (2004).
[2] B. J. Spencer and J. Tersoff, Appl. Phys. Lett. **77**, 2533 (2000).
[3] B. J. Spencer and J. Tersoff, Phys. Rev. B **63**, 205424 (2001).
[4] F. K. LeGoues, M. C. Reuter, J. Tersoff, M. Hammar, and R. M. Tromp, Phys. Rev. Lett. **73**, 300 (1994).
[5] M. Hammar, F. K. LeGoues, J. Tersoff, M. C. Reuter, and R. M. Tromp, Surf. Sci. **349**, 129 (1996).
[6] A. Rastelli, M. Stoffel, A. Malachias, T. Merdzhanova, G. Katsaros, K. Kern, T. Metzger, and O. Schmidt, Nano Lett. **8**, 1404 (2008).
[7] T. Merdzhanova, S. Kiravittaya, A. Rastelli, M. Stoffel, U. Denker, and O. G. Schmidt, Phys. Rev. Lett. **96**, 226103 (2006).
[8] *X-Ray and Neutron Diffraction in Nonideal Crystals*, edited by M. A. Krivoglaz (Springer-Verlag, Berlin, 1996).
[9] U. Pietsch, V. Holý, and T. Baumbach, *High-Resolution X-Ray Scattering from Thin Films to Lateral Nanostructures*, 2nd ed. (Springer, New York, 2004).
[10] A. Malachias, R. Magalhaes-Paniago, B. R. A. Neves, W. N. Rodrigues, M. V. B. Moreira, H.-D. Pfannes, A. G. de Oliveira, S. Kycia, and T. H. Metzger, Appl. Phys. Lett. **79**, 4342 (2001).
[11] M. I. Richard, T. H. Metzger, V. Holý, and K. Nordlund, Phys. Rev. Lett. **99**, 225504 (2007).
[12] D. Y. Ryu, K. Shin, E. Drokenmuller, C. J. Hawker, and T. P. Russell, Science **308**, 236 (2005).
[13] J. Stangl, A. Daniel, V. Holý, T. Roch, G. Bauer, I. Kegel, T. H. Metzger, and T. Wiebach, Appl. Phys. Lett. **79**, 1474 (2001).
[14] M. Stoffel, A. Rastelli, J. Tersoff, T. Merdzhanova, and O. G. Schmidt, Phys. Rev. B **74**, 155326 (2006).
[15] I. Kegel, T. H. Metzger, P. Fratzl, J. Peisl, A. Lorke, J. M. Garcia, and P. M. Petroff, Europhys. Lett. **45**, 222 (1999).
[16] T. U. Schülli, M. Stoffel, A. Hesse, J. Stangl, R. T. Lechner, E. Wintersberger, M. Sztucki, T. H. Metzger, O. G. Schmidt, and G. Bauer, Phys. Rev. B **71**, 035326 (2005).
[17] V. Favre-Nicolin, Computer code NANOMAD (private communication).
[18] J. Hodeau, V. Favre-Nicolin, S. Bos, H. Renevier, E. Lorenzo, and J. Berar, Chem. Rev. **101**, 1843 (2001).
[19] T. U. Schülli, G. Vastola, M. I. Richard, A. Malachias, G. Renaud, F. Uhlík, F. Montalenti, G. Chen, L. Miglio, F. Schäffler, and G. Bauer, Phys. Rev. Lett. **102**, 025502 (2009).
[20] G. Renaud, P. Guénard, and A. Barbier, Phys. Rev. B **58**, 7310 (1998).
[21] O. Robach, G. Renaud, and A. Barbier, Phys. Rev. B **60**, 5858 (1999).
[22] D. K. Satapathy, V. M. Kaganer, B. Jenichen, W. Braun, L. Däweritz, and K. H. Ploog, Phys. Rev. B **72**, 155303 (2005).
[23] G. Renaud, A. Barbier, and O. Robach, Phys. Rev. B **60**, 5872 (1999).
[24] M. Hÿtch, E. Snoeck, and R. Kilaas, Ultramicroscopy **74**, 131 (1998).
[25] P. Ehrhart, H. Trinkaus, and B. C. Larson, Phys. Rev. B **25**, 834 (1982).
[26] *Theory of Dislocations*, edited by J. P. Hirth and J. Lothe, 2nd ed. (Krieger, Florida, 1992).

[27] A. Malachias, T. U. Schülli, G. Medeiros-Ribeiro, L. G. Cancado, M. Stoffel, O. G. Schmidt, T. H. Metzger, and R. Magalhaes-Paniago, Phys. Rev. B **72**, 165315 (2005).

[28] *X-ray Diffraction*, edited by B. E. Warren (Dover Publications, 1969).

[29] F. H. Stillinger and T. A. Weber, Phys. Rev. B **31**, 5262 (1985).

[30] K. Nordlund, U. Beck, T. H. Metzger, and J. R. Patel, Appl. Phys. Lett. **76**, 846 (2000).

[31] S. A. Chaparro, Y. Zhang, J. Drucker, D. Chandrasekhar, and D. J. Smith, J. Appl. Phys. **87**, 2245 (2000).

[32] G. Capellini, M. D. Seta, and F. Evangelisti, Mater. Sci. Eng. B **89**, 184 (2002).

[33] Z. Zhong, W. Schwinger, F. Schäffler, G. Bauer, G. Vastola, F. Montalenti, and L. Miglio, Phys. Rev. Lett. **98**, 176102 (2007).

[34] T.-S. Yoon, H.-M. Kim, K.-B. Kim, D. Y. Ryu, T. P. Russell, Z. Zhao, J. Liu, and Y.-H. Xie, J. Appl. Phys. **102**, 104306 (2007).

[35] Q. Li, B. Pattada, S. R. J. Brueck, S. Hersee, and S. M. Han, J. Appl. Phys. **98**, 073504 (2005).